Fast Magnetic Reconnection with Turbulence in High Lundquist Number Limit

Liping Yang[1,2] , Hui Li[2] , Fan Guo[2] , Xiaocan Li[2] , Shengtai Li[2], Jiansen He[3] , Lei Zhang[4], and Xueshang Feng[1]
[1] SIGMA Weather Group, State Key Laboratory for Space Weather, National Space Science Center, Chinese Academy of Sciences, Beijing, 100190, People's Republic of China; lpyang@swl.ac.cn
[2] Theoretical Division, MS B284, Los Alamos National Laboratory, Los Alamos, NM 87545, USA
[3] School of Earth and Space Sciences, Peking University, Beijing, 100871, People's Republic of China
[4] Qian Xuesen Laboratory of Space Technology, Beijing, 100190, People's Republic of China
Received 2020 July 6; revised 2020 September 1; accepted 2020 September 9; published 2020 September 24

Abstract

We use extensive 3D resistive MHD simulations to study how large-scale current sheets will undergo fast reconnection in the high Lundquist number S limit (above $\sim 10^4$), when the system is subject to different externally driven turbulence levels and the self-generated turbulence produced by 3D reconnection dynamics. We find that the normalized global reconnection rate ~ 0.01–0.13 is weakly dependent on S. Global reconnection with the classic inflow/outflow configurations is observed, and 3D flux ropes are hierarchically formed and ejected from reconnection regions. A statistical separation of the reconnected magnetic field lines follows a superdiffusive behavior, from which the rate is measured to be very similar to that obtained from the mixing of tracer populations. We find that the reconnection rate scales roughly linearly with the turbulence level during the peak of reconnection. This scaling is consistent with the turbulence properties produced by both the externally driven and self-generation processes. These results imply that large-scale thin current sheets tend to undergo rigorous reconnection.

Unified Astronomy Thesaurus concepts: Solar magnetic reconnection (1504); Interplanetary turbulence (830); Computational methods (1965); Solar corona (1483)

1. Introduction

Fast magnetic reconnection (at a fraction of Alfvén speed V_A) is often invoked to explain energetic events such as solar/stellar flares, substorms in the magnetosphere of Earth and other planets, coronal mass ejections, sawtooth crashes in fusion plasmas, and other astrophysical systems (Priest & Forbes 2007; Lazarian et al. 2020). During reconnection, oppositely directed magnetic field lines restructure themselves, resulting in a rapid conversion of magnetic energy into kinetic energy of bulk flows, and thermal and nonthermal particles (e.g., Drake et al. 2006).

In the limit of resistive magnetohydrodynamics (MHD) description, the classical Sweet–Parker (SP) model (Sweet 1958; Parker 1957) predicts a rather slow reconnection rate proportional to $S^{-1/2}$, where $S = L V_A/\eta$ is the Lundquist number, η is the plasma resistivity, and L is the characteristic length of the system. Many alternatives to speed up the reconnection have been investigated (Priest & Forbes 2007; Lin et al. 2015; Cassak & Shay 2012; Loureiro & Uzdensky 2016). A major advance came through studies related to the resistive tearing instability (Biskamp 1986; Loureiro et al. 2007; Bhattacharjee et al. 2009; Huang & Bhattacharjee 2010; Uzdensky et al. 2010; Ni et al. 2012; Lin & Ni 2018). In the high S limit, it is found that, above a critical $S \sim 10^4$, the two-dimensional (2D) thin SP current sheets (CSs) become violently unstable to the hierarchical formation and ejection of plasmoids (Loureiro et al. 2007), producing a nearly resistivity-independent reconnection rate around $0.01V_A$.

Fast magnetic reconnection in the presence of 3D turbulence is a critically important process in space and astrophysical plasmas (Matthaeus & Lamkin 1986; Lazarian & Vishniac 1999; Fan et al. 2004; Kowal et al. 2009; Loureiro et al. 2009; Daughton et al. 2011; Eyink et al. 2011; Guo et al. 2015; Oishi et al. 2015; Takamoto et al. 2015; Wyper & Hesse 2015; Huang & Bhattacharjee 2016; Beresnyak 2017; Kowal et al. 2017; Pisokas et al. 2018; Li et al. 2019; Ye et al. 2020), with some interesting

support from observation (Fu et al. 2017; Cheng et al. 2018; He et al. 2018; Chitta & Lazarian 2020). Broadly speaking three types of configurations have been studied in some detail, depending on what "free energy" is available. The first is on how externally driven (or decaying) turbulence affects the reconnection of a preexisting CS(s) (e.g., Matthaeus & Lamkin 1986; Lazarian & Vishniac 1999; Kowal et al. 2009; Loureiro et al. 2009; Kowal et al. 2012). The 3D MHD simulations have mostly been done in the small S ($\sim$a few thousand) limit, though the externally driven turbulence with relatively large amplitude can greatly enhance the reconnection rate up to $\sim 0.1V_A$. The second is similar to the first type except that the turbulence is self-generated from instabilities associated with the preexisting CS(s) or additional instabilities due to reconnection (e.g., Oishi et al. 2015; Huang & Bhattacharjee 2016; Beresnyak 2017; Kowal et al. 2017, 2020). The 3D MHD simulations in this category with S up to a few times 10^5 have shown that the reconnection rate is slightly slower, averaging around a few percent of V_A. Note that these two types of studies could differ in important ways because the available free energy in the second case is primarily from the initial CS only, whereas in the first case both the injected turbulence and the CS contribute to the available energy for dissipation. In particular, Lazarian & Vishniac (1999, hereafter LV99) and Eyink et al. (2011, hereafter ELV11) provided the basic theoretical model on such turbulent reconnection. The third is to begin with the injected turbulence only without a preexisting semi-global CS(s). The turbulence cascade will produce CSs at intermediate scales that could undergo reconnection. 2D MHD simulations (Dong et al. 2018; Walker et al. 2018) and 3D kinetic simulations (e.g., Makwana et al. 2015) appear to lend support to these ideas. In fact, the dual process of CS formation by turbulence cascade and the back-reaction on turbulence by the possible reconnection of such sheets have led to new models of MHD turbulence with reconnection (e.g., Boldyrev & Loureiro 2017; Loureiro & Boldyrev 2017). Note that the available free energy in this case is only the injected

turbulence, very different from the first two types. Overall, the interplay among the externally injected turbulence versus the self-generated turbulence, and the preexisting CS(s) versus the self-generated CSs makes it challenging to build a comprehensive theory. Numerical simulations tend to have a limited dynamic range to fully resolve several critical issues revealed by these theoretical models (see a recent discussion in Lazarian et al. (2020)).

In this work, we use a set of 3D compressible MHD simulations to systematically examine how the reconnection rate in the low plasma $\beta = 0.1$ condition scales with the strength of turbulence as well as S. Our most important conclusion is that, in systems with an initial large-scale CS, the 3D reconnection rate can range between 0.01–$0.1 V_A$, and scales roughly linearly with the turbulent Alfvén Mach number $M_A \sim 0.06$–0.32. The rate is weakly dependent on S in the high S limit. Flux ropes, as the 3D version of the 2D plasmoid instability, are frequently formed and ejected along the thin CSs. Magnetic field line tracing yields superdiffusive behavior. The turbulence is a combination of the externally driven and the self-generated fluctuations, but with a second-order structure function different from the incompressible MHD turbulence theory by Goldreich & Sridhar (1995).

2. Numerical MHD Model

The isothermal resistive MHD equations in a periodic cube with a side length of $L = 2\pi$ are solved:

$$\frac{\partial \rho}{\partial t} + \nabla \cdot (\rho \boldsymbol{u}) = 0, \tag{1}$$

$$\frac{\partial \rho \boldsymbol{u}}{\partial t} + \nabla \cdot \left[\rho \boldsymbol{u}\boldsymbol{u} + \left(p + \frac{1}{2}\boldsymbol{B}^2\right)\boldsymbol{I} - \boldsymbol{B}\boldsymbol{B}\right] = \nu \nabla^2 \boldsymbol{u} + \rho \boldsymbol{f}_v, \tag{2}$$

$$\frac{\partial \boldsymbol{B}}{\partial t} + \nabla \cdot (\boldsymbol{u}\boldsymbol{B} - \boldsymbol{B}\boldsymbol{u}) = \eta \nabla^2 \boldsymbol{B}, \tag{3}$$

$$\frac{\partial s_i}{\partial t} + \nabla \cdot (s_i \boldsymbol{u}) = 0. \tag{4}$$

Here, ρ is the mass density; p is the thermal pressure; $\boldsymbol{u}$ is the velocity; $\boldsymbol{B}$ denotes the magnetic field; t is time; ν is the viscosity; η is the magnetic resistivity; s_i ($i = 1, 2$) are the densities of the tracer populations (Yang et al. 2013); $\boldsymbol{f}_v$ is a random large-scale driving force, applied in Fourier space at $k < 3.5$ (Yang et al. 2017, 2018). We have used $\nu = \eta$ in all simulations.

The initial magnetic field has a Harris configuration with two thin CSs as $\boldsymbol{B} = B_0\left[\tanh(\frac{x - x_1}{w}) - \tanh(\frac{x - x_2}{w})\right]\hat{y} - B_0\hat{y}$, where B_0 is the asymptotic magnetic field, $x_1 = \pi/2$ and $x_2 = 3\pi/2$ are the initial positions of the CSs, and the parameter w is set to satisfy the SP scaling of $2w/L \simeq S^{-1/2}$. Initially, the density profile is set to maintain a uniform total (thermal plus magnetic) pressure, velocity is zero, and plasma β is about 0.1. Due to the broadening likely caused by turbulence, the CS layer during evolution is typically resolved with more than 10 cells. The externally driven turbulence is characterized by $\boldsymbol{f}_v$. When $|\boldsymbol{f}_v| = 0$, the velocity is initially seeded with a random noise of amplitude 10^{-3}. Simulation parameters are listed in Table 1, in which N is grid number in one direction. M_A is Alfvén Mach number defined as $M_A = u_{rms}/V_A$ with u_{rms} being the rms amplitude of the velocity at the peak reconnection, and V_A the

Table 1
Reconnection MHD Simulations

Run	N^3	S	M_A	$|f_v|$	CSs
A1	2048^3	2.3×10^5	0.322	0.30	Yes
A2	1024^3	6.3×10^4	0.305	0.30	Yes
A3	1024^3	1.5×10^4	0.304	0.30	Yes
A4	1024^3	4.8×10^3	0.302	0.30	Yes
B1	2048^3	2.3×10^5	0.192	0.10	Yes
B2	1024^3	6.3×10^4	0.185	0.10	Yes
B3	1024^3	1.5×10^4	0.183	0.10	Yes
B4	1024^3	4.8×10^3	0.180	0.10	Yes
C1	2048^3	2.3×10^5	0.098	0.01	Yes
C2	1024^3	6.3×10^4	0.092	0.01	Yes
C3	1024^3	1.5×10^4	0.089	0.01	Yes
C4	1024^3	4.8×10^3	0.084	0.01	Yes
D1	2048^3	2.3×10^5	0.072	No	Yes
D2	1024^3	6.3×10^4	0.067	No	Yes
D3	1024^3	1.5×10^4	0.060	No	Yes
D4	1024^3	4.8×10^3	0.056	No	Yes
E	1024^3	6.3×10^4	0.421	0.30	No

Alfvén speed based on the initial magnetic field B_0 and the average density. Run E only has a uniform magnetic field without any initial CSs. We use the Athena code (Gardiner & Stone 2005; Stone et al. 2008) for simulations. Specifically, we apply the approximate Riemann solver of Harten–Lax–van Leer discontinuities (HLLD) to the calculation of the numerical fluxes, a third-order piecewise parabolic method (PPM) to the reconstruction, MUSCL-Hancock (VL) Integrator to the time integration, and the constrained transport (CT) algorithm to ensure the divergence-free state of the magnetic field.

3. Numerical Results

We find that all runs containing initial CSs will undergo global reconnection characterized by inflow/outflow patterns. Figure 1 shows that the two initially parallel thin CSs are now strongly deformed by the externally driven turbulence while undergoing 3D reconnection. The width of the CSs also demonstrates thinning and thickening at various places. A number of magnetic field lines are plotted and three typical behaviors are observed: first, field lines that are relatively smooth and arch-looking start at one side of a CS and end up at the other side of the same CS, indicating reconnection accompanied with X-points and large opening angles for reconnected lines; second, field lines that are far away from the CSs go through the box without reconnection; and third, field lines start at one side of a CS but trace out in twisted trajectories (possibly flux ropes) and end up far away from the starting points.

To calculate the 3D reconnection rate, we use the method described in Daughton et al. (2014), which employs the mixing of tracer populations originating from separate sides of a CS as a proxy to identify the reconnection region and track the evolution of magnetic flux. We solve Equation (4) using two tracer species s_1 and s_2. The initial values of s_1 and s_2 are such that on one side of a CS, $s_1 = -1$ and otherwise 0, whereas on the other side of the same CS, $s_2 = 1$ and otherwise 0. As reconnection proceeds, the populations tagged by s_1 and s_2 will interpenetrate and a mixing fraction f_e can be defined as
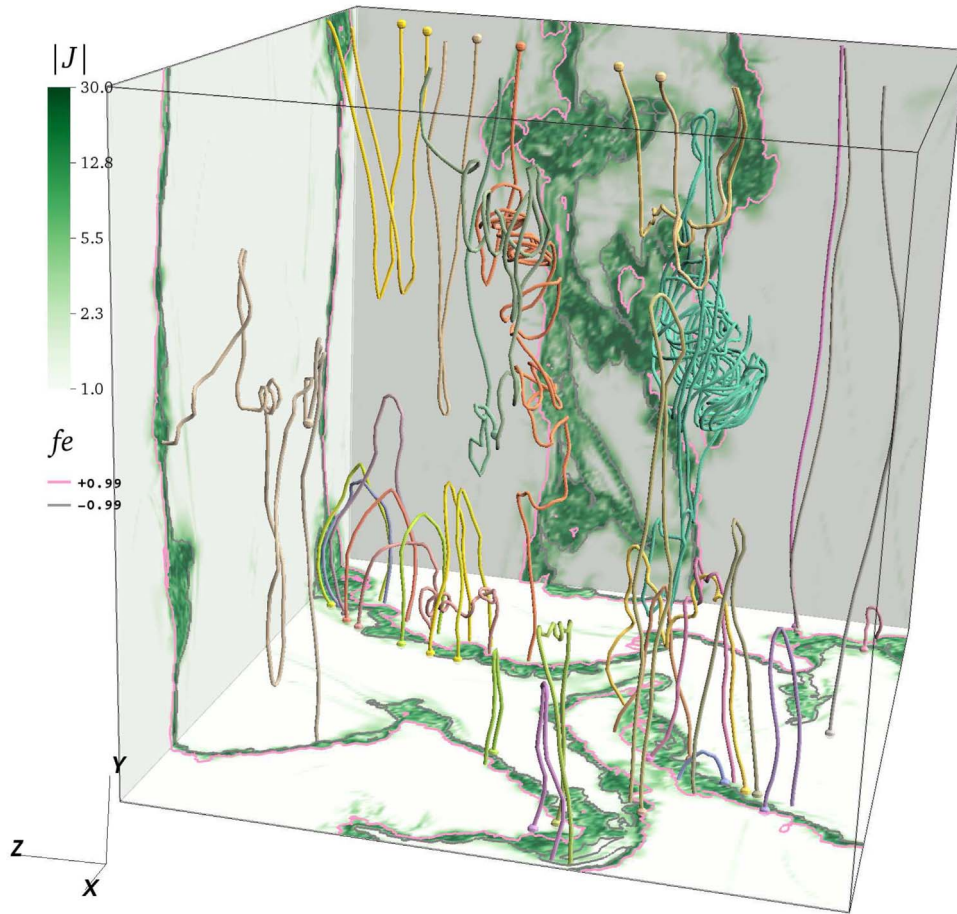
Figure 1. Spatial distribution of the total current density (|J|) for Run A1 at $t = 2.0$. Only intersections with the three bounding planes are shown. The colored lines denote sample magnetic field lines. The pink and gray contour lines show $f_e = 0.99$ and -0.99, respectively.

$f_e = \frac{|s_1| - |s_2|}{|s_1| + |s_2|}$, which will vary continuously from $f_e = -1$ on one side of the CS to $f_e = 1$ to the other side of the same CS. In Figure 1, we can see that the contours of f_e enclose the strong |J| layers quite well, correlating strong mixing/reconnection with strong |J|. The 3D reconnection rate is calculated according to the time derivative of the unreconnected magnetic flux $\frac{\partial \Phi}{\partial t}$ within the regions with $f_e < -f_c$ or $f_e > f_c$ as $\frac{\partial \Phi}{\partial t}$ is equal to the line integral of the electric field along the surfaces of $f_e = -f_c$ or $f_e = f_c$ due to the periodic boundary condition. We have also calculated the change rate of the magnetic flux within the regions with $f_e \geqslant -f_c$ and $f_e \leqslant f_c$ and found that it is an order of magnitude smaller than $\frac{\partial \Phi}{\partial t}$. Therefore, it can be thought that the flux entering into the reconnection region is dissipated quickly. Because the boundaries that separate $f_e \neq \pm 1$ regions from $f_e = \pm 1$ regions are quite sharp, the calculated reconnection rate is insensitive if f_c is in the range 0.9–0.995 (Daughton et al. 2014). Here, we choose $f_c = 0.99$. The calculated reconnection rate grows first as the reconnection starts, reaching a maximum after a few Alfvén times, then gradually decreasing.

To further demonstrate global reconnection in our simulations, we show in Figure 2 that the classic X−point inflow/outflow configuration is approximately preserved in the turbulent reconnection. The plasma originating from separate sides of the CSs flows into the reconnection region with an inflow speed of $\sim 0.15 V_A$; meanwhile, the outflows along the CSs appear to reach values of $\sim \pm V_A$ (from which the global reconnection rate could also be estimated to be ~ 0.15 for Run A1). There seems to be one major reconnection X-point in the left CS near $y = 0$, whereas plasmoid-like chains with large |J_z| and |B_z| are visible in the right CS. In addition, in the left CS between $y = 0$ and 2, the strong shear in $|\Delta V_y|/(|B_y|/\sqrt{\rho}) > 2$ might indicate the excitation of Kelvin–Helmholtz instability (Miura & Pritchett 1982; Kowal et al. 2020).

To understand the current sheet structure in more detail, we evaluate the current sheet width for Run A1 at different times, which is defined when |J_z| comes to e^{-1} of its maximum. In panels (f) and (h) of Figure 2, we give two examples of the current sheet width at $t = 2.0$, in which the horizontal dashed lines cut through the |J_z| structure, and two vertical solid lines mark the current sheet width, which is about 0.033 and is resolved by about 10 cells. In panel (i), we show the evolution of the current sheet width. It starts with a width of about 0.073 (resolved by about 24 cells), and undergoes a thinning process, but it remains broader than that predicted by the SP scaling, presumably due to the turbulence. Overall, the current sheet width is adequately resolved numerically.

We now discuss the turbulence properties in further detail. Panel (a) of Figure 3 shows that the power spectra of kinetic energy displays a $\sim -5/3$ power law for the different Runs A1—D1, although the weaker turbulence runs seem to show slightly flatter spectra. Because the plasma $\beta \sim 0.1$, the turbulence is sub-Alfvénic but becoming transonic for
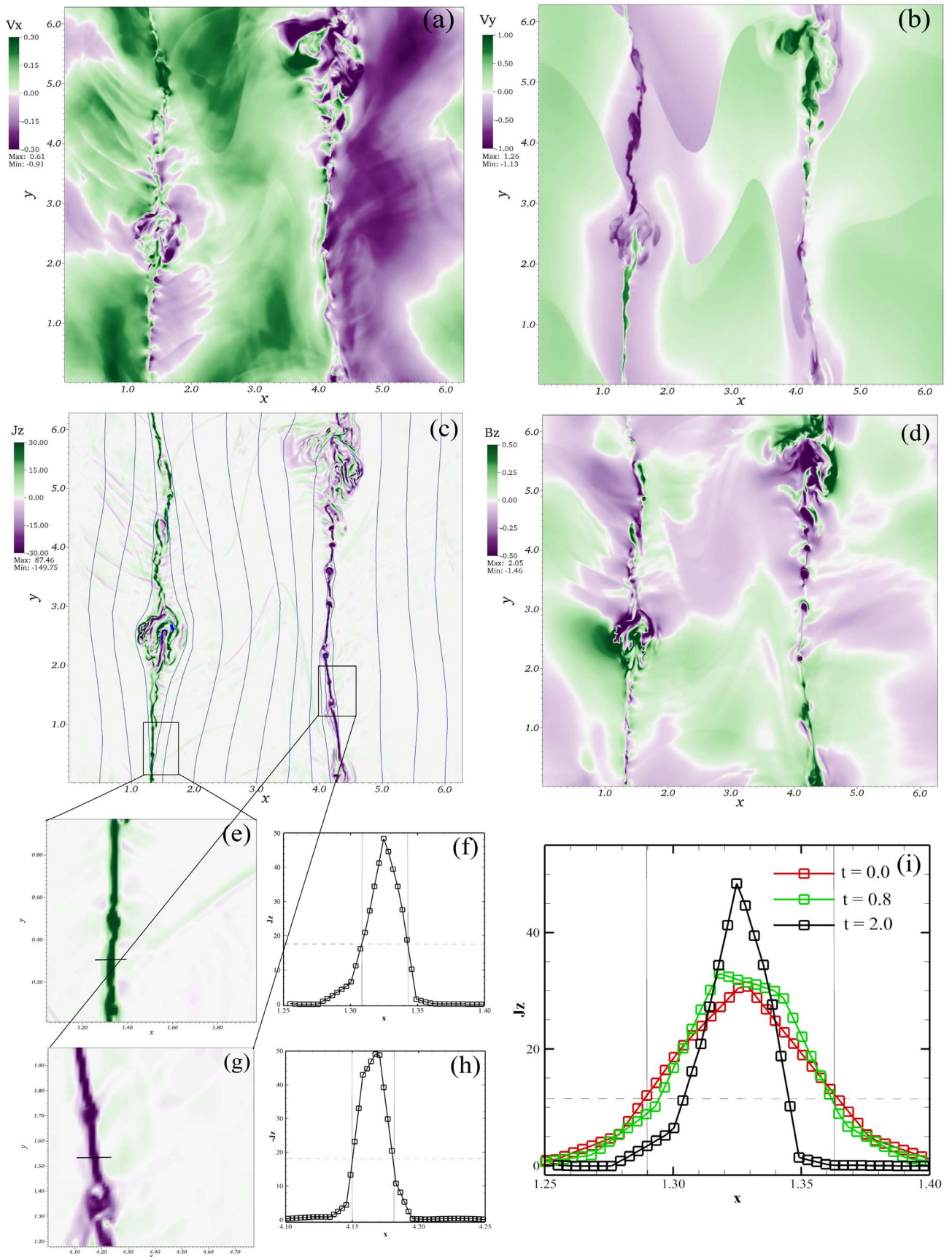
Figure 2. Spatial distributions of a 2D x–y slice at $z = 1.2$ of the velocity components V_x (a) and V_y (b), the current density J_z component along with the (blue lines) magnetic field lines projected into the x–y plane (c), and the magnetic field component B_z (d) for Run A1 at $t = 2.0$. Panels (e) and (g) zoom in around two strong $|J_z|$ regions; panels (f) and (h) show the one-dimensional (1D) distribution of $|J_z|$ along the black lines in panels (e) and (g); and panel (i) shows the 1D distribution of $|J_z|$ at different times, with the black line being the same as that in panel (f). The cell size is ~ 0.003 in this run.
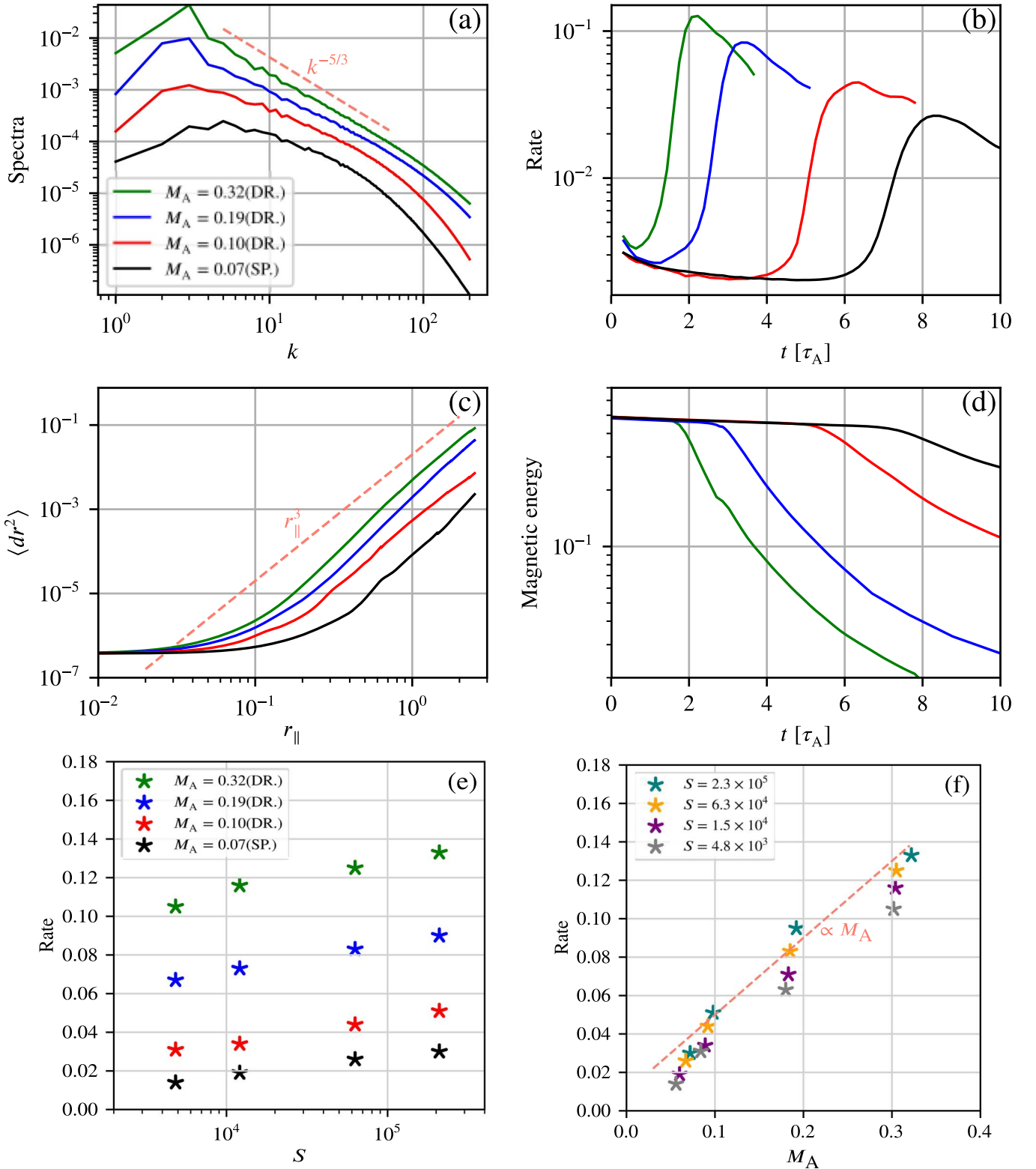
Figure 3. Power spectra of kinetic energy (a), global reconnection rate (b), diffusion of reconnecting magnetic field lines (c), and magnetic energy evolution (d) for different levels of turbulence driving for Runs A1, B1, C1, and D1, global reconnection rates as a function of the Lundquist number S for different values of the Alfvén Mach number M_A (e) and as a function of M_A for different S (f). Quantities in panels (a) and (c) are calculated at the time when the global reconnection rate shown in panel (b) reaches its respective maximum.

$M_A \sim 0.3$ (Run A1). The rate for the strongest external driving turbulence (Run A1) is about $0.128V_A$, which is consistent with the estimate measured from inflow and outflow speeds shown in Figure 2. The rate for spontaneous turbulent reconnection (Run D1) is about $0.025V_A$, which is basically consistent with the results by Oishi et al. (2015), Beresnyak (2017), and Kowal et al. (2017). In addition, the sharp rise of the rates corresponds well with the rapid decrease of the total magnetic energy within

the simulation box, indicating that the fast reconnection has dissipated a significant fraction of the available magnetic energy (by ~50% to nearly 100%).

To see the connection between the reconnection rates and the diffusion of turbulent magnetic fields, we measure the separation dr of numerous pairs of field lines as a function of $r_\parallel$ (the distance along the field lines) like Beresnyak (2013). These pairs start at random positions within the reconnection regions with $|f_e| < 1$. Panel (c) of Figure 3 shows the relationship between $\langle dr^2 \rangle$ and $r_\parallel$ in which 10^5 field line pairs are used for statistical averaging. A stochastic separation of magnetic field lines follows a superdiffusion behavior. As the reconnection proceeds, $\langle dr^2 \rangle$ rises. At the turbulence injection scale, $r_\parallel \sim 3$, we can calculate the field line separation rate as $\langle dr^2 \rangle^{0.5}/r_\parallel$, similar to Lazarian & Vishniac (1999) and Eyink et al. (2011). The rates for Runs A1, B1, C1, and D1 are 0.123, 0.093, 0.036, and 0.023, respectively, which are similar to the maximum of the global reconnection rates obtained from the mixing of traced populations as shown in panel (b). However, when $r_\parallel > 0.1$, the standard deviation of the averaged rates for Runs A1, B1, C1, and D1 increases to be the same order of magnitude as the average value $\langle dr^2 \rangle$.

Applying these analyses to all the runs (except Run E) listed in Table 1, we summarize the dependence of 3D reconnection rates (taken at the peak of their evolution) on S and M_A. As shown in panel (e) of Figure 3, the reconnection rate shows a rather weak increasing trend as S increases. Even higher S values are needed to see if the reconnection rate becomes weakly dependent on S. Note that the variation of reconnection rates for a given M_A is within ~50% as S goes from 4.8×10^3 to 2.3×10^5. Assuming that the reconnection rate stays below V_A for very large S, it is reasonable to expect that the dependence of the reconnection rate on S should be rather weak. Consequently, we conclude that the reconnection rate is weakly dependent on S when S is large.

The reconnection rate, however, does show a clear dependence on the level of turbulence. Panel (f) of Figure 3 shows that the rate scales roughly linearly with the turbulent M_A. This slope is obtained by mostly using points from simulation Runs A–C with the same S. The weak dependence on S can also be seen. In addition, it seems that the "spontaneous" Run D cannot be regarded as simply an extrapolation to zero f_v, as its reconnection rates are a bit lower than the extrapolation from Runs A–C. We suggest that this is due to a fundamental change of the turbulence properties between Run A and Run D. For Run A, the turbulence mostly experiences forward cascades, whereas for Run D, the fluctuations are first injected at the CS width scales, then undergo both forward and inverse cascades (Bowers & Li 2007).

To investigate the turbulence properties in more detail, we analyze the anisotropy of the turbulence using Runs A1, B1, and C1. We have calculated the second-order structure functions (SFs) of velocity in terms of parallel $l_\parallel$ and perpendicular displacement $l_\perp$ with respect to the local magnetic field reference frame and the correspondence between $l_\parallel$ and $l_\perp$ by equating SF values in parallel and perpendicular directions (Beresnyak 2017; Kowal et al. 2017). The results are shown in Figures 4(a) and (b). To facilitate a comparison, the results for the fully developed turbulence without the initial large-scale CSs (Run E) are also presented in Figures 4(c) and (d).

The resulting SFs clearly display that turbulent eddies are elongated along the local magnetic field direction for Run A1. For pure turbulence Run E, eddies become increasingly more

anisotropic at smaller scales, basically conforming to the Goldreich & Sridhar prediction (Goldreich & Sridhar 1995). Comparing the properties from Runs A1 and E, however, we see that the anisotropy in Run A1 is weaker than that in Run E, showing a power-law scaling with $l_\parallel \propto l_\perp^{6/5}$ for all the scales captured in the simulation. Although both Run B1 and Run C1 have smaller Alfvén Mach numbers than Run A1, the anisotropy in them displays a power-law scaling closer to $l_\parallel \propto l_\perp^{6/5}$ than $l_\parallel \propto l_\perp^{2/3}$. This may be owing to the fact that how the turbulence is produced in our current models is different from the traditional Goldreich & Sridhar (1995) model, as discussed in the next section.

4. Discussion

The results presented here extend the previous studies in 3D turbulent MHD reconnection by systematically examining the previous unexplored parameter space in both S and M_A. On the one hand, we find good consistency with the previous results in the low S and/or low M_A regimes such as the reconnection rates ranging between 0.01 and $0.1 V_A$. On the other hand, we find two new conclusions: one is that the reconnection rate is weakly dependent on S in the large S limit and the other is that the reconnection rate scales roughly linearly with the turbulent M_A. The weak dependence on S is consistent with both the turbulent reconnection model (Lazarian & Vishniac 1999) and plasmoid-mediated reconnection model (Loureiro et al. 2007; Bhattacharjee et al. 2009; Huang & Bhattacharjee 2010; Uzdensky et al. 2010).

The new, linear scaling relationship we find between the reconnection rate and the strength of turbulence is different from the M_A^2 scaling given in Lazarian & Vishniac (1999). Our turbulence properties are also different from Goldreich & Sridhar (1995). Using the anisotropy scaling from our simulations, we can derive our new reconnection rate dependence on M_A in the context of the turbulent reconnection theory (Lazarian & Vishniac 1999; Eyink et al. 2011). From the constant energy transfer rate of $\dot{\xi} \sim \frac{v_k^2}{\tau_{nl}} \sim v_k^4 \frac{k_\perp^2}{k_\parallel V_A}$ (Lazarian & Vishniac 1999) and the simulation result of $k_\parallel \sim k_\perp^{6/5}$, we can get that $v_{k_{\perp l}} \sim v_{k_{\perp L}} k_{\perp L}^{1/5}/k_{\perp l}^{1/5}$, with L being the energy injection scale, l being the inertial scale, $k_{\perp L} \sim 1/L$, $k_{\perp l} \sim 1/l$, and $v_{k_{\perp L}}$ as well as $v_{k_{\perp l}}$ being the corresponding perpendicular fluctuating velocities. As a pair of field lines with an initial distance of $l_\perp^{(0)}$ separate at the rate $\frac{d}{ds} l_\perp \sim \frac{\delta b_{\perp l}}{B_0} \sim \frac{\delta v_{\perp l}}{V_A}$ (Eyink et al. 2011), one finds that $\frac{d}{ds} l_\perp \sim \frac{v_{k_{\perp L}} k_{\perp L}^{1/5}}{k_{\perp l}^{1/5} V_A}$, that is, $l_\perp \sim M_A^{5/4} k_{\perp L}^{1/4} s^{5/4}$ with $M_A = v_{k_{\perp L}}/V_A$. We can estimate the rate by $l_\perp/s \sim M_A^{5/4}$. Given that the inertial range is limited and the turbulence is not steady, our numerical result of the rate $\propto M_A$ is approximately consistent with this relationship.

The nature of turbulence from Runs A to D likely undergoes significant changes. The turbulence in our simulations come from both the external driven origin as well as the self-generated origin. In Run A1, the reconnection rate is high and the flow from the 3D reconnection is quite significant (with the outflow speeds reaching V_A as shown in Figure 2). Both the presence of large-scale reconnection CSs and the flows associated with reconnection are affecting the turbulence. In fact, according to Table 1, comparing Run A2 and Run E where the external driving f_v is the same (and the same numerical resolution), the turbulent M_A is actually larger in the
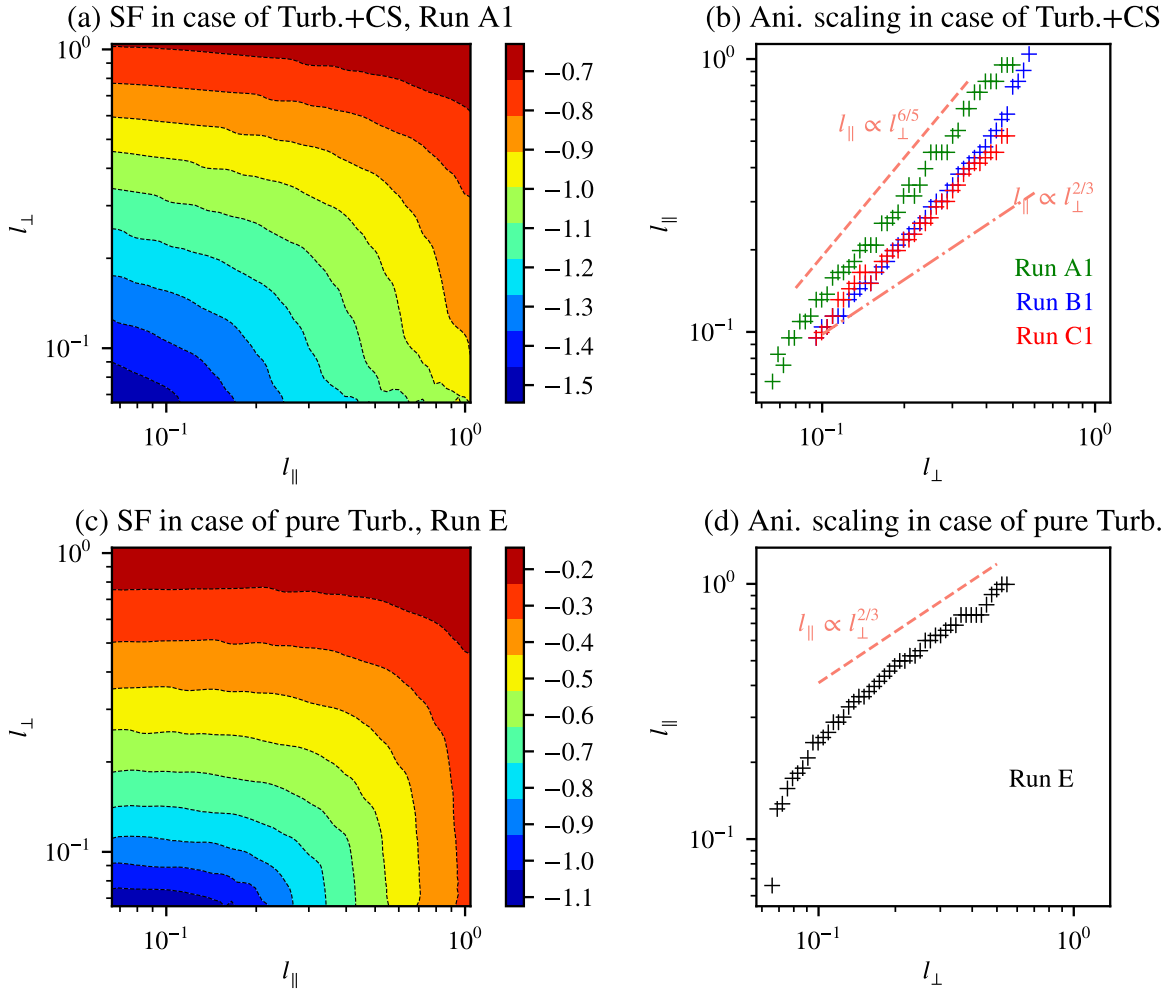
Figure 4. Second-order structure functions (SFs) of velocity from the fully developed turbulence with the large-scale CSs (a) and without the initial large-scale CSs (pure turbulence) (c). Panels (b) and (d): relationships between semimajor axis $l_\parallel$ and semiminor axis $l_\perp$ of contours in panels (a) and (c), which measure the scale dependency of turbulent eddy anisotropy.

pure turbulence run (0.421) than that in the reconnection run (0.305). Because the self-generated turbulence likely undergoes both forward and inverse cascades, its spectral properties and anisotropy will not follow the Goldreich & Sridhar theory, especially when the turbulence properties are examined at just a few Alfvén times. In addition, our simulations are in the low β situation (initially at 0.1) with an aim to model the solar coronal environment, whereas most previous simulations have mostly explored the higher β limit (Oishi et al. 2015; Beresnyak 2017; Kowal et al. 2017). According to the results of Kowal et al. (2017), the anisotropy degree and scaling depend on the plasma β, and larger β conditions tend to yield scalings closer to the Goldreich & Sridhar theory.

The self-generated turbulence/fluctuations likely have several origins. The first is from the resistive tearing instabilities on relatively smaller scales of CS thickness; the second is from the Kelvin–Helmholtz instability in the localized outflow regions, again on CS thickness scales; the third is from the "collisions" of outflows (see $y \sim 2 - 3$ in Figure 2). Although these processes can all in principle produce turbulence, our simulations probably do not have enough spatial separation to see the development of all these turbulences. Overall, the third process likely contributes the most to the self-generated turbulence.

Because the "spontaneous" runs can already produce $M_A \geqslant 0.06$ with a reconnection rate $\sim 0.01 V_A$, this implies that, in space and astrophysical systems and to the extent that periodic boundary conditions can be approximately true, large-scale current sheets with high S will tend to be destroyed within several Alfvén transient times of the system.

ORCID iDs

Liping Yang https://orcid.org/0000-0003-4716-2958
Hui Li https://orcid.org/0000-0003-3556-6568
Fan Guo https://orcid.org/0000-0003-4315-3755
Xiaocan Li https://orcid.org/0000-0001-5278-8029

Jiansen He ⑩ https://orcid.org/0000-0001-8179-417X
Xueshang Feng ⑩ https://orcid.org/0000-0001-8605-2159

References

Beresnyak, A. 2013, ApJL, 767, L39
Beresnyak, A. 2017, ApJ, 834, 47
Bhattacharjee, A., Huang, Y.-M., Yang, H., & Rogers, B. 2009, PhPl, 16, 112102
Biskamp, D. 1986, PhFl, 29, 1520
Boldyrev, S., & Loureiro, N. F. 2017, ApJ, 844, 125
Bowers, K., & Li, H. 2007, PhRvL, 98, 035002
Cassak, P. A., & Shay, M. A. 2012, SSRv, 172, 283
Cheng, X., Li, Y., Wan, L. F., et al. 2018, ApJ, 866, 64
Chitta, L. P., & Lazarian, A. 2020, ApJL, 890, L2
Daughton, W., Nakamura, T. K. M., Karimabadi, H., Roytershteyn, V., & Loring, B. 2014, PhPl, 21, 052307
Daughton, W., Roytershteyn, V., Karimabadi, H., et al. 2011, NatPh, 7, 539
Dong, C., Wang, L., Huang, Y.-M., Comisso, L., & Bhattacharjee, A. 2018, PhRvL, 121, 165101
Drake, J. F., Swisdak, M., Che, H., & Shay, M. A. 2006, Natur, 443, 553
Eyink, G. L., Lazarian, A., & Vishniac, E. T. 2011, ApJ, 743, 51
Fan, Q.-L., Feng, X.-S., & Xiang, C.-Q. 2004, PhPl, 11, 5605
Fu, H. S., Vaivads, A., Khotyaintsev, Y. V., et al. 2017, GeoRL, 44, 37
Gardiner, T. A., & Stone, J. M. 2005, JCoPh, 205, 509
Goldreich, P., & Sridhar, S. 1995, ApJ, 438, 763
Guo, F., Liu, Y.-H., Daughton, W., & Li, H. 2015, ApJ, 806, 167
He, J., Zhu, X., Chen, Y., et al. 2018, ApJ, 856, 148
Huang, Y.-M., & Bhattacharjee, A. 2010, PhPl, 17, 062104
Huang, Y.-M., & Bhattacharjee, A. 2016, ApJ, 818, 20
Kowal, G., Falceta-Gonçalves, D. A., Lazarian, A., & Vishniac, E. T. 2017, ApJ, 838, 91
Kowal, G., Falceta-Gonçalves, D. A., Lazarian, A., & Vishniac, E. T. 2020, ApJ, 892, 50
Kowal, G., Lazarian, A., Vishniac, E. T., & Otmianowska-Mazur, K. 2009, ApJ, 700, 63
Kowal, G., Lazarian, A., Vishniac, E. T., & Otmianowska-Mazur, K. 2012, NPGeo, 19, 297
Lazarian, A., Eyink, G. L., Jafari, A., et al. 2020, PhPl, 27, 012305
Lazarian, A., & Vishniac, E. T. 1999, ApJ, 517, 700
Li, X., Guo, F., Li, H., Stanier, A., & Kilian, P. 2019, ApJ, 884, 118
Lin, J., & Ni, L. 2018, in Electric Currents in Geospace and Beyond, ed. A. Keiling, O. Marghitu, & M. Wheatland (Washington, DC: AGU), 239
Lin, J., Murphy, N. A., Shen, C., et al. 2015, SSRv, 194, 237
Loureiro, N. F., & Boldyrev, S. 2017, PhRvL, 118, 245101
Loureiro, N. F., Schekochihin, A. A., & Cowley, S. C. 2007, PhPl, 14, 100703
Loureiro, N. F., & Uzdensky, D. A. 2016, PPCF, 58, 014021
Loureiro, N. F., Uzdensky, D. A., Schekochihin, A. A., Cowley, S. C., & Yousef, T. A. 2009, MNRAS, 399, L146
Makwana, K. D., Zhdankin, V., Li, H., Daughton, W., & Cattaneo, F. 2015, PhPl, 22, 042902
Matthaeus, W. H., & Lamkin, S. L. 1986, PhFl, 29, 2513
Miura, A., & Pritchett, P. L. 1982, JGR, 87, 7431
Ni, L., Ziegler, U., Huang, Y.-M., Lin, J., & Mei, Z. 2012, PhPl, 19, 072902
Oishi, J. S., Mac Low, M.-M., Collins, D. C., & Tamura, M. 2015, ApJL, 806, L12
Parker, E. N. 1957, JGR, 62, 509
Pisokas, T., Vlahos, L., & Isliker, H. 2018, ApJ, 852, 64
Priest, E., & Forbes, T. 2007, Magnetic Reconnection (Cambridge: Cambridge Univ. Press)
Stone, J. M., Gardiner, T. A., Teuben, P., Hawley, J. F., & Simon, J. B. 2008, ApJS, 178, 137
Sweet, P. A. 1958, in IAU Symp., 6, Electromagnetic Phenomena in Cosmical Physics, ed. B. Lehnert (Cambridge: Cambridge Univ. Press), 123
Takamoto, M., Inoue, T., & Lazarian, A. 2015, ApJ, 815, 16
Uzdensky, D. A., Loureiro, N. F., & Schekochihin, A. A. 2010, PhRvL, 105, 235002
Walker, J., Boldyrev, S., & Loureiro, N. F. 2018, Phys. Rev. E, 98, 033209
Wyper, P. F., & Hesse, M. 2015, PhPl, 22, 042117
Yang, L., He, J., Peter, H., et al. 2013, ApJ, 770, 6
Yang, L., He, J., Tu, C., et al. 2017, ApJ, 836, 69
Yang, L., Zhang, L., He, J., et al. 2018, ApJ, 866, 1
Ye, J., Cai, Q., Shen, C., et al. 2020, ApJ, 897, 64